ARTICLES
https://doi.org/10.1038/s41566-018-0241-1

nature photonics

Terahertz dynamics of electron–vibron coupling in single molecules with tunable electrostatic potential

Shaoqing Du[1]*, Kenji Yoshida[1], Ya Zhang[1,4], Ikutaro Hamada[2,5] and Kazuhiko Hirakawa[1,3]*

Clarifying electronic and vibronic properties at the individual molecule level provides key insights for future chemistry, nanoelectronics and quantum information technologies. However, information obtained by conventional single-molecule transport measurements is based on time-averaged properties. Here, we report on terahertz (THz) spectroscopy of single fullerene molecules by using a single-molecule transistor geometry. From the time-domain THz autocorrelation measurements, we obtained THz spectra associated with the THz-induced centre-of-mass oscillation of the molecules. The observed spectra reflect the potential profile experienced by the molecule on the metal surface when the number of electrons on the molecule fluctuates by one during the single-electron tunnelling process. Such an ultra-high sensitivity to the electronic/vibronic structures of a single molecule on the addition/removal of a single electron has been achieved as a result of using THz spectroscopy in the single-molecule transistor geometry. This scheme provides an opportunity to investigate the ultrafast THz dynamics of subnanometre-scale systems.

Terahertz spectroscopy has been developed as a powerful tool for clarifying vibrational dynamics of various kinds of molecule[1–3]. Because of the long-wavelength nature of the THz electromagnetic waves (typically, ~100 µm), however, spectral information is obtained only for an ensemble average of a large number of molecules. It has been a formidable challenge to far exceed the diffraction limit and focus the THz radiation on single molecules. Furthermore, the number of mobile charges that can absorb THz radiation in a single molecule is very low, which makes THz absorption extremely small. Here, we report THz spectroscopy of single molecules by using the single-molecule transistor (SMT) geometry[4–7]. The SMT is a structure in which a single molecule is captured in a subnanometre gap created between the source and drain metal electrodes fabricated on a field plate. Using the source and drain electrodes separated by a subnanometre gap as a THz antenna, we focus THz radiation onto a single fullerene molecule trapped in the nanogap electrodes. Furthermore, we can detect a very small absorption by measuring the THz-induced photocurrent by the same electrodes.

Terahertz spectroscopy using nanogap electrodes

We fabricated C_{60} SMTs by using the electrical break junction (EBJ) method[8,9]. Figure 1a shows a scanning electron microscope image of the sample structure used in this work. A 10-nm-thick NiCr layer, which serves as a semi-transparent back-gate electrode, was deposited on a high-resistivity Si substrate, and a 30-nm-thick Al_2O_3 gate-insulation film was grown by atomic layer deposition. We formed thin gold nanojunctions, which were used for forming the source and drain electrodes, on the surface of the wafer by the shadow evaporation technique. To achieve a good coupling efficiency between the THz radiation and the single molecule, we employed a bowtie-antenna shape for the source and drain electrodes (Fig. 1a). Since the fabrication yield of SMTs is typically only a few per cent, we fabricated nine junctions on a chip in an area of 200 × 200 µm^2. The chip was then glued with varnish on a hemispherical silicon lens to tightly focus the THz radiation on the bowtie antenna. A dilute toluene solution of C_{60} molecules was deposited on the surface of the gold nanojunctions and dried off with nitrogen gas. The sample was then mounted in a vacuum space of a ^{4}He cryostat. We applied the feedback-controlled EBJ process to the metal nanojunctions and fabricated source–drain electrodes separated by a subnanometre gap (Fig. 1b)[8–10]. Details of the feedback control of the EBJ process have been described elsewhere[10]. All the measurements were performed at ~4.6 K in a vacuum.

By using the nanogap electrodes[11–13], THz radiation can be tightly focused onto a single molecule. Furthermore, the local THz field in the nanogap is enhanced by a factor of ~10^5 by the plasmonic effect of the metal electrodes[13–15]. In this work, we faced a problem in performing spectroscopy on a single molecule by using broadband THz bursts excited by femtosecond laser pulses; the SMTs are very slow devices due to their high tunnel resistances and it is impossible to read ultrafast current changes. To overcome this problem, we adopted the time-domain THz autocorrelation measurements[16–19] (Fig. 1c). Using a beam splitter, we split the laser beam into two parts and created double laser pulses. A surface of an InAs wafer was consecutively pumped by the femtosecond laser pulses and the time-correlated THz double pulses were generated. By recording the photocurrent induced by the THz double pulses as a function of the time interval between the THz pulses, τ, we obtained interferograms of the photocurrent induced in the single molecule by THz radiation (quasi-autocorrelation measurement; see Methods for more details). We used a mode-locked Ti:sapphire laser with a central wavelength at 810 nm, pulse duration ~10 fs and repetition frequency of 76 MHz. The output power of the laser was

---

[1]Institute of Industrial Science, University of Tokyo, Meguro-ku, Tokyo, Japan. [2]Center for Green Research on Energy and Environmental Materials, National Institute for Materials Science, Tsukuba, Japan. [3]Institute for Nano Quantum Information Electronics, University of Tokyo, Meguro-ku, Tokyo, Japan. [4]Present address: Institute of Engineering, Tokyo University of Agriculture and Technology, Koganei, Tokyo, Japan. [5]Present address: Department of Precision Science and Technology, Osaka University, Suita, Osaka, Japan. *e-mail: sqdu@iis.u-tokyo.ac.jp; hirakawa@iis.u-tokyo.ac.jp

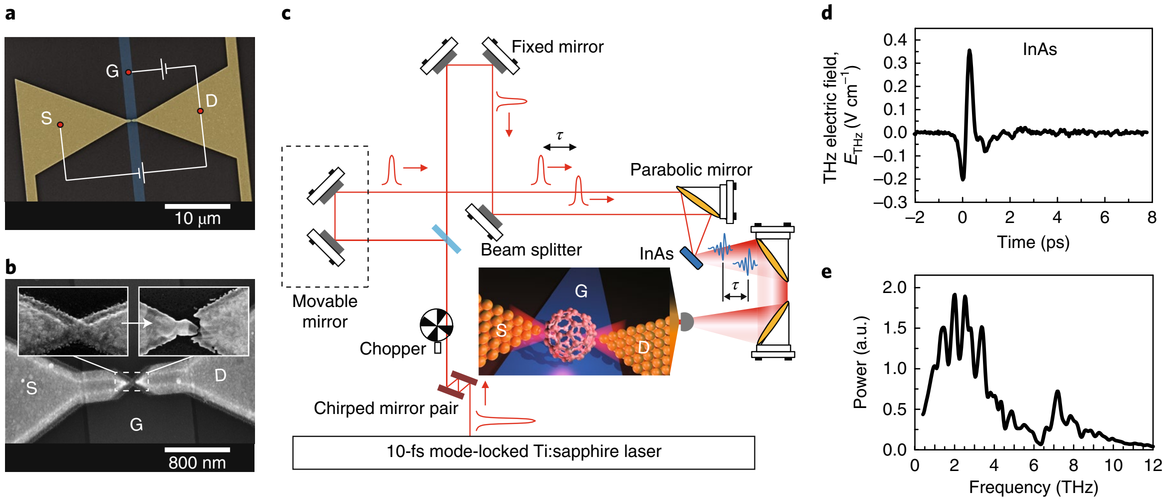

Fig. 1 | Set-up for single-molecule terahertz spectroscopy. a, Scanning electron microscopy (SEM) image of a SMT sample with a bowtie antenna structure. S, D and G denote the source, drain and gate electrodes of the SMT, respectively. **b**, SEM images of the nanojunction region before and after the electrical break-junction process. A single molecule is captured in the created nanogap. **c**, Schematic illustration of the experimental set-up. Femtosecond laser pulses (centre wavelength, 810 nm; pulse duration, ~10 fs; repetition rate, 76 MHz) are split into two parts and focused on a THz emitter (InAs wafer). The generated THz bursts are collected and focused onto the SMT mounted in a ^{4}He cryostat. **d**, THz waveform used in the measurements. THz pulses were generated by pumping the surface of an InAs wafer by 10-fs laser pulses from a mode-locked Ti:sapphire laser. The THz waveform was measured by using the electro-optic (EO) sampling method. The EO sensor used in the measurement was a 700-μm-thick (110) cut ZnTe. The THz pulse has a monocycle waveform and maximum THz field ~0.4 V cm^{-1}. **e**, Spectrum of the THz pulses measured by using a wideband Si bolometer in the quasi-autocorrelation geometry (see Methods). The THz spectrum extends up to 12 THz.

typically 500 mW. The generated THz waveform was measured by electro-optic (EO) sampling in a 700-μm-thick (110) ZnTe crystal. As shown in Fig. 1d, the THz pulses had a monocycle waveform and their peak THz field was approximately 0.4 V cm^{-1}. Since the bandwidth of the 700-μm-thick EO sensor is limited up to 3 THz, we characterized the emitted THz radiation also by using a wideband Si bolometer in the quasi-autocorrelation geometry. As shown in Fig. 1e, the power spectrum of the emitted THz radiation extends up to 12 THz.

We performed transport measurements to examine whether we captured a single molecule in the nanogap (see Supplementary Information for the sample statistics). Figure 2a shows a colour-coded differential conductance (dI_{DS}/dV_{DS}) map of a C_{60} SMT plotted as a function of the source–drain voltage, V_{DS}, and the gate voltage, V_G (Coulomb stability diagram). A crossing pattern in the diagram indicates that this device operates as a single-electron transistor. Furthermore, the excitation of an internal vibrational mode at ~33 meV (ref. [20]), which is intrinsic to the C_{60} molecule, was observed in the Coulomb stability diagram, confirming that a single C_{60} molecule was indeed trapped in the nanogap of the electrodes and served as a Coulomb island.

Terahertz-induced vibron-assisted tunnelling

After identifying the molecule from transport measurements, we illuminated the sample with THz pulses by setting $\tau \gg 10$ ps and searched for the time-averaged THz-induced photocurrent. By sweeping V_G while applying a small source–drain voltage ($V_{DS} = 0.1$ mV), we measured the THz-induced photocurrent as a function of V_G. The black curve in Fig. 2b is the sample conductance in the dark condition, whereas the red trace is the measured THz-induced photocurrent. The peak of the black curve corresponds to the charge degeneracy point of the C_{60} SMT. A very small, but finite photocurrent of the order of 100 fA was observed near the charge degeneracy point. Recently, single-molecule THz spectroscopy has been performed by using a scanning tunnelling microscope tip to focus the THz radiation onto a single pentacene molecule[21]. Although site-selective THz spectroscopy by imaging the molecular orbitals using scanning tunnelling microscopy was possible[21], the advantage of our SMT geometry is that we can precisely control the electrostatic potential and the number of electrons on the molecule by the gate electric fields. Another important difference is that, since the incident THz field is weak (<0.4 V cm^{-1}) in our experiment, the effect of instantaneous bias change induced across the C_{60} molecule is negligibly small (on the order of 1 mV). Therefore, our experiment was performed in a regime very different from that reported in ref. [21] and provides complementary information.

Figure 2c shows an interferogram of the THz-induced photocurrent measured for a C_{60} SMT when the gate voltage was set at the peak position of the photocurrent ($V_G = 0.024$ V). The curve is the interferogram obtained by averaging 10 scans. A clear centre peak and interference feature can be seen. By calculating the Fourier spectrum of the interferogram, we obtained a THz spectrum for a C_{60} SMT. Two peaks are observed at around 2 meV and 4 meV (Fig. 2e). We analysed the inerferogram shown in Fig. 2c and decomposed the waveform into the 2 meV (500 GHz)- (blue curve) and 4 meV (1 THz)- (green curve) oscillation components (Fig. 2d). The oscillation of the 4-meV component is clearly visible in the photocurrent waveform, particularly at around 1 ps. It should be noted that a THz vibrational spectrum is obtained even for a single molecule when the SMT geometry is used. Similar sharp peaks were also observed for an endohedral metallofullerene Ce@C_{82} SMT (Fig. 2f).

The low-energy excitations observed for a C_{60} SMT originate from the vibron-assisted tunnelling promoted by the THz-induced centre-of-mass oscillation of the C_{60} molecule. Vibron-assisted inelastic tunnelling has been observed in tunnelling spectroscopy measurements[4]. In the transport experiments, the molecular vibration is excited by injecting tunnel electrons and the excited-state lines are visible only inside the single-electron tunnelling region of the Coulomb stability diagrams. In the THz spectroscopy measurements, molecular vibrations are excited not only by the tunnelling electrons but also by the impulsive THz fields generated by the femtosecond laser pulses. Because of the broadband THz

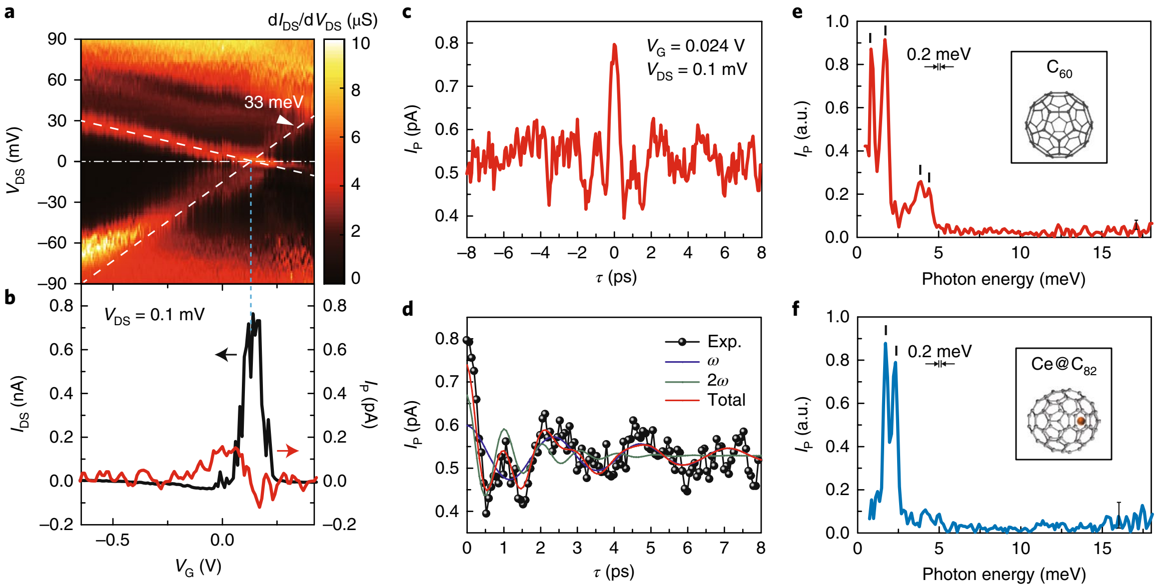

Fig. 2 | Teraherz autocorrelation measurements of a single C_{60} molecule. a, Coulomb stability diagram of a C_{60} SMT. White dashed lines are guides to the eye for the boundaries of the Coulomb diamonds. The excited-state line at 33 meV is an internal vibrational mode of the C_{60} molecule. The blue dashed line indicates the gate voltage position of the charge degeneracy point in the single-electron tunnelling (also see **b**). **b**, The single-electron tunnelling current I_{DS} (black curve) and the THz-induced photocurrent I_P (red curve) as a function of V_G measured at $V_{DS} = 0.1$ mV. **c**, Quasi-autocorrelation trace (interferogram) of the THz-induced photocurrent measured at the peak of the photocurrent ($V_G = 0.024$ V, $V_{DS} = 0.1$ mV). τ is the time difference between the two consecutive femtosecond laser pulses. The quasi-autocorrelation trace was obtained by averaging data for eight scans. **d**, The interferogram for $\tau > 0$, replotted from **c**. The dots are the measured data points. The blue and green curves are fitting curves for the fundamental frequency ω (500 GHz) and the second-harmonic frequency 2ω (1 THz) oscillation components, respectively. The red curve shows the total of the ω and 2ω components. The peak splitting (see main text) was not included in the fitting. **e**, Fourier spectrum of the interferogram shown in **c**. The spectrum exhibits sharp peaks at ~2 meV and ~4 meV. Additional data are shown in the Supplementary Information. **f**, THz spectrum for a single-Ce@C_{82} SMT. Two sharply split peaks are observed at around 2 meV.

excitation, the centre-of-mass oscillation of the C_{60} molecule is excited and creates new tunnelling paths for electrons, that is, the vibron-assisted tunnelling processes, as schematically shown in Fig. 3a,b. When the lowest unoccupied molecular orbital (LUMO) level is above the Fermi level of the electrodes, an electron in the electrodes cannot enter the molecule in the dark condition. However, when the centre-of-mass oscillation of the C_{60} molecules is excited by the THz radiation, an electron in the electrode can absorb a vibron and tunnel into the molecule (vibron-assisted tunnelling). In this case, the electron number on the molecule increases from N to $N+1$, that is, the molecule changes its state from C_{60} to C_{60}^-. Although N cannot be determined only from the present experiment, N is most likely to be zero. Figure 3b shows a vibron-assisted tunnelling-out process when the highest occupied molecular orbital (HOMO) level is below the Fermi level of the electrode. In this case, the electron on the HOMO level cannot leave the molecule in the dark condition, but, with THz illumination, it can escape the molecule via vibron-assisted tunnelling. Furthermore, we can roughly estimate the quality (Q) factor of the C_{60} molecular vibration to be approximately 3–5, although the linewidths of the sharp peaks are affected by the resolution of the experimental set-up. This means that an electron that hops on the C_{60} molecule resides on the molecule at least for about 3–5 cycles of vibration and then leaves the molecule. We have estimated the electron tunnelling time, τ_T, through the C_{60} molecule to be 8 ps from the sample conductance in the dark condition (~7 μS), using the following relationship[22]

$$G_{\max} = \frac{e^2}{4k_B T}\frac{\Gamma^l \Gamma^r}{\Gamma^l + \Gamma^r} \tag{1}$$

and assuming $\Gamma^l \approx \Gamma^r \approx 1/\tau_T$. Here, e is the elementary charge, k_B the Boltzmann constant, T the temperature and $G_{\max}$ the conductance of the Coulomb peak. Γ^l (Γ^r) is the tunnel coupling between the molecule and the left (right) electrode. The obtained τ_T is consistent with the electron dwell time on the molecule determined from the Q factor.

Splitting of vibron peaks

An interesting observation is that the vibron peaks around 2 meV and 4 meV are finely split into two. The magnitudes of the peak splittings at around 2 meV and 4 meV are 0.8 meV and 0.6 meV, respectively. We measured five C_{60} SMTs in total and four of them showed the same splitting feature. In addition, a similar peak splitting was observed in the THz spectrum of a Ce@C_{82} SMT. The excited-state lines due to molecular vibrations in the Coulomb stability diagrams originate from the Franck–Condon effect[23–25]. As schematically shown in Fig. 3d, the overlap of the vibrational wavefunctions gives the tunnelling probability of an electron for the transition between the N and $N+1$ states (the Franck–Condon principle)[23–25]. When the charge state changes from the N to the $N+1$ electron state, the equilibrium position of the molecule may shift by δ. This shift induces not only the diagonal transitions but also the off-diagonal transitions between the vibrational states of the N and $N+1$ charge states, giving rise to multiple excited-state lines in the Coulomb stability diagrams[25] (see Supplementary Information). In previous discussions[4,23–25], the vibrational frequencies of the molecule for the N and $N+1$ charge states were assumed to be the same. However, this may not be the case in actual systems, that is, the van der Waals potential felt by a C_{60} molecule on the gold surface may depend on the charge state of the molecule.

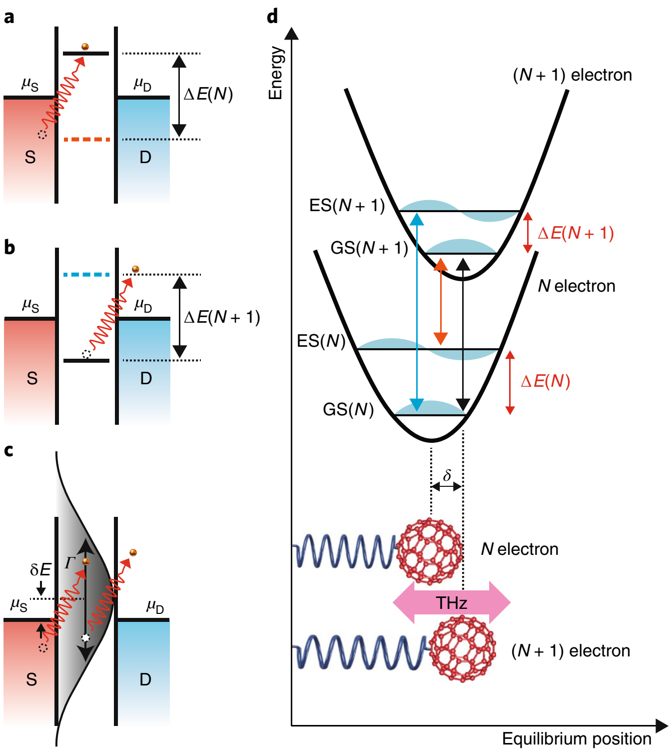

Fig. 3 | Vibron-assisted tunnelling in a C_{60} single-molecule transistor. **a**, Tunnel-in process. When the lowest unoccupied molecular orbital (LUMO) level is above the Fermi level of the electrodes, an electron in the electrode can absorb a vibron and jump into the molecule when molecular vibration is excited by THz electromagnetic fields. μ_S and μ_D denote the electrochemical potentials in the source and the drain electrodes, respectively. The red dashed line denotes the *N* electron vibrational ground state. **b**, Tunnel-out process. When the highest occupied molecular orbital (HOMO) level in the molecules is below the Fermi level of the electrode, the electron can absorb a vibron and jump out of the molecule when molecular vibration is excited by THz electromagnetic fields. The blue dashed line denotes the $N+1$ electron vibrational excited state. **c**, The energy band diagram at the peak of the photocurrent ($V_G = 0.024$ V, $V_{DS} = 0.1$ mV) in Fig. 2b. The Lorentzian curve schematically illustrates the electronic levels in the molecule. The broadening of the LUMO level, Γ, is determined to be ~10 meV from the Coulomb stability diagram shown in Fig. 2a. The centre of the LUMO level is located 4 meV above the Fermi levels in the electrodes (δE). Because Γ is larger than δE, both the vibron-assisted tunnel-in process and the tunnel-out process are possible. **d**, Schematic illustration of the vibronic energy diagram of the C_{60} molecule in the nanogap. The C_{60} molecule experiences the van der Waals potential on the surface of the gold electrode and performs the centre-of-mass oscillation. The parabolas and the wavefunctions in the diagram schematically illustrate the vibronic energy states for the *N* and $N+1$ electron states. When an electron is added to the C_{60} molecule, the equilibrium position of the molecule shifts by δ. The vibronic energies for the *N* and $N+1$ electron states are expressed as $\Delta E(N)$ and $\Delta E(N+1)$, respectively. Owing to the resonant absorption of THz photons, electron tunnelling via the GS(N) ↔ ES($N+1$) and ES(N) ↔ GS($N+1$) transitions becomes possible and THz-induced photocurrent is generated even in the Coulomb gap. GS, ground state; ES, excited state.

To gain insight into the vibrational and electronic states of the C_{60} molecule in the SMT geometry, we performed van der Waals inclusive[26] density functional theory (DFT) calculations of neutral and negatively charged C_{60} on a Au(111) surface, which correspond to the *N* and $N+1$ charged states, respectively. The method of the calculation is described in the Supplementary Information. In Fig. 4, we plot the interaction energy curves for neutral and negatively charged C_{60} on a Au (111) surface. The equilibrium C_{60}–surface distance is 0.243 nm and the vibrational energy, $\hbar\omega$, is 4.1 meV. The calculated vibrational energy is larger than the value obtained by THz spectroscopy (~2 meV), presumably because the counter electrode is lacking in the model system used in the present DFT calculation. We found that, when C_{60} is negatively charged, the system gets destabilized, because the antibonding state between the LUMO of C_{60} and the substrate state is partially occupied[27]. Accordingly, the equilibrium distance becomes longer by 0.011 nm and the vibrational energy is lowered by 0.7 meV. This result is the opposite to a simple expectation when only the image-charge force in the metal electrode is considered, because the Coulomb force generated by the image-charges attracts the molecule towards the metal electrode. Our calculations suggest that the vibrational energy depends on the charge state and thus the splitting of the vibron-assisted tunnelling peak is expected. Indeed, the magnitude of the observed splitting (0.6–0.8 meV) is in good agreement with the calculated change in the vibrational energy (0.7 meV).

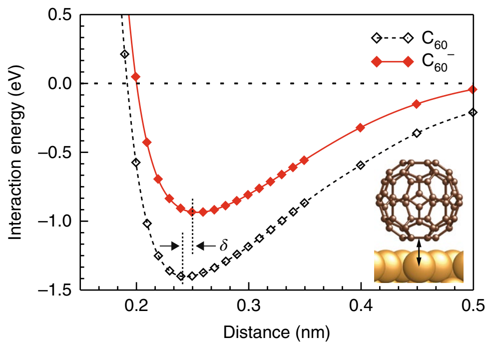

Fig. 4 | Calculated interaction energy for a C_{60} molecule on a gold surface. Open and filled diamonds display the interaction energies calculated as a function of the molecule–surface distance for C_{60} and C_{60}^- on a Au(111) surface, respectively. The molecule–surface distance is defined as the difference between the average *z* coordinates of the bottom carbon atoms of C_{60} and the surface gold atoms, as denoted by the double-headed arrow in the inset. For the C_{60} molecule on the gold surface (the *N*-electron state), the characteristic vibronic energy, $\hbar\omega$, is 4.1 meV. When an electron is added to the C_{60} molecule (the $N+1$-electron state), the equilibrium distance becomes larger by 0.011 nm. At the same time, the characteristic vibronic energy becomes smaller by 0.7 meV.

The reasons why we observe the vibron peaks for the *N* and $N+1$ charge state at the same time in the THz spectrum are explained in the following. As seen in Fig. 2b, the peak of the THz-induced photocurrent is located on the negative-side tail of the Coulomb peak ($V_G = 0.024$ V). At this gate voltage, the LUMO is estimated to be 4 meV above the Fermi level, using the lever-arm factor, $\alpha = 0.03$, in this sample. On the other hand, as shown in Fig. 2a, the tunnel peak of this SMT is very broad (~10 meV), much broader than the energy difference between the Fermi level and the LUMO. Therefore, an electron can hop onto or out of the molecule at this bias condition and the number of electrons on the molecule can fluctuate (either *N* or $N+1$), as schematically illustrated in Fig. 3c.

Conclusion

We have demonstrated that THz spectroscopy can detect an ultrafast oscillatory motion of a single C_{60} molecule. Low-energy vibrational modes are observed at around 2 meV and 4 meV and are attributed to the THz-induced centre-of-mass nanomechanical oscillation of the C_{60} molecule. Furthermore, we have found that the observed THz peaks are finely split into two, reflecting the difference in the van der Waals potential profile experienced by the C_{60} molecule on the metal surface when the number of electrons on the molecule fluctuates between N and $N+1$ during the single-electron tunnelling process. Such an ultra-high sensitivity to the electronic/vibronic structures of a single molecule on charging/discharging a single electron has been achieved by using metal source–drain electrodes separated by a subnanometre gap as a THz antenna and detecting the THz-induced photocurrent.

Methods

Methods, including statements of data availability and any associated accession codes and references, are available at https://doi.org/10.1038/s41566-018-0241-1.

Received: 12 February 2017; Accepted: 31 July 2018;

References

1. van Exter, M., Fattinger, C. & Grischkowsky, D. Terahertz time-domain spectroscopy of water vapor. *Opt. Lett.* **14**, 1128–1130 (1989).
2. Beard, M. C., Turner, G. M. & Schmuttenmaer, C. A. Measuring intramolecular charge transfer via coherent generation of THz radiation. *J. Phys. Chem. A* **106**, 878–883 (2002).
3. Jepsen, P. U. & Clark, S. J. Precise ab-initio prediction of terahertz vibrational modes in crystalline systems. *Chem. Phys. Lett.* **442**, 275–280 (2007).
4. Park, H. et al. Nanomechanical oscillations in a single-C_{60} transistor. *Nature* **407**, 57–60 (2000).
5. Kubatkin, S. et al. Single-electron transistor of a single organic molecule with access to several redox states. *Nature* **425**, 698–701 (2003).
6. Osorio, E. A. et al. Electronic excitations of a single molecule contacted in a three-terminal configuration. *Nano Lett.* **7**, 3336–3342 (2007).
7. de Leon, N. P., Liang, W., Gu, Q. & Park, H. Vibrational excitation in single-molecule transistors: deviation from the simple Franck–Condon prediction. *Nano Lett.* **8**, 2963–2967 (2008).
8. Park, H., Lim, A. K. L., Alivisatos, A. P., Park, J. & McEuen, P. L. Fabrication of metallic electrodes with nanometer separation by electromigration. *Appl. Phys. Lett.* **75**, 301–303 (1999).
9. Strachan, D. et al. Controlled fabrication of nanogaps in ambient environment for molecular electronics. *Appl. Phys. Lett.* **86**, 043109 (2005).
10. Umeno, A. & Hirakawa, K. Nonthermal origin of electromigration at gold nanojunctions in the ballistic regime. *Appl. Phys. Lett.* **94**, 162103 (2009).
11. Shibata, K., Umeno, A., Cha, K. M. & Hirakawa, K. Photon-assisted tunneling through self-assembled InAs quantum dots in the terahertz frequency range. *Phys. Rev. Lett.* **109**, 077401 (2012).
12. Zhang, Y. et al. Terahertz intersublevel transitions in single self-assembled InAs quantum dots with variable electron numbers. *Nano Lett.* **15**, 1166–1170 (2015).
13. Yoshida, K., Shibata, K. & Hirakawa, K. Terahertz field enhancement and photon-assisted tunneling in single-molecule transistors. *Phys. Rev. Lett.* **115**, 138302 (2015).
14. Seo, M. A. et al. Terahertz field enhancement by a metallic nano slit operating beyond the skin-depth limit. *Nat. Photon.* **3**, 152–156 (2009).
15. Ward, D. R., Huser, F., Pauly, F., Cuevas, J. C. & Natelson, D. Optical rectification and field enhancement in a plasmonic nanogap. *Nat. Nanotech.* **5**, 732–736 (2010).
16. Kersting, R., Unterrainer, K., Strasser, G., Kauffmann, H. F. & Gornik, E. Few-cycle THz emission from cold plasma oscillations. *Phys. Rev. Lett.* **79**, 3038–3041 (1997).
17. Shimada, Y., Hirakawa, K., Odnoblioudov, M. & Chao, K. A. Terahertz conductivity and possible Bloch gain in semiconductor superlattices. *Phys. Rev. Lett.* **90**, 046806 (2003).
18. Cocker, T. L. et al. An ultrafast terahertz scanning tunnelling microscope. *Nat. Photon.* **7**, 620–625 (2013).
19. Yoshioka, K. et al. Real-space coherent manipulation of electrons in a single tunnel junction by single-cycle terahertz electric fields. *Nat. Photon.* **10**, 762–765 (2016).
20. Heid, R., Pintschovius, L. & Godard, J. M. Eigenvectors of internal vibrations of C_{60}: theory and experiment. *Phys. Rev. B* **56**, 5925–5936 (1997).
21. Cocker, T. L., Peller, D., Yu, P., Repp, J. & Huber, R. Tracking the ultrafast motion of a single molecule by femtosecond orbital imaging. *Nature* **539**, 263–267 (2016).
22. Beenakker, C. W. J. Theory of Coulomb-blockade oscillations in the conductance of a quantum dot. *Phys. Rev. B* **44**, 1646–1656 (1991).
23. Leturcq, R. et al. Franck–Condon blockade in suspended carbon nanotube quantum dots. *Nat. Phys.* **5**, 327–331 (2009).
24. Burzurí, E. et al. Franck–Condon blockade in a single-molecule transistor. *Nano Lett.* **14**, 3191–3196 (2014).
25. Koch, J. & von Oppen, F. Franck–Condon blockade and giant Fano factors in transport through single molecules. *Phys. Rev. Lett.* **94**, 206804 (2005).
26. Hamada, I. van der Waals density functional made accurate. *Phys. Rev. B* **89**, 121103 (2014).
27. Hamada, I., Araidai, M. & Tsukada, M. Origin of nanomechanical motion in a single-C_{60} transistor. *Phys. Rev. B* **85**, 121401 (2012).

Acknowledgements

We thank Y. Arakawa for discussions on single-molecule spectroscopy and S. Ishida for his technical help in the fabrication process. This work is supported by KAKENHI (Grant-in-Aid for Scientific Research) on Innovative Areas 'Science of hybrid quantum systems' (15H05868) from the Ministry of Education, Culture, Sports, Science and Technology, Japan (MEXT), KAKENHI from Japan Society for the Promotion of Science (JSPS) (16H06709 and 17H01038), the Project for Developing Innovation Systems of MEXT, and the Canon Science Foundation.

Author contributions

S.Q.D. fabricated the single-molecule transistor samples and carried out the THz measurements. K.H. conceived and supervised the project. K.Y. supported the transport measurements and Y.Z. provided assistance with the THz spectroscopy. I.H. carried out the DFT calculations. S.Q.D., I.H. and K.H. wrote the manuscript with contributions from all authors. All authors contributed to discussions.

Competing interests

The authors declare no competing interests.

Additional information

Supplementary information is available for this paper at https://doi.org/10.1038/s41566-018-0241-1.

Reprints and permissions information is available at www.nature.com/reprints.

Correspondence and requests for materials should be addressed to S.Q.D. or K.H.

Methods

Quasi-autocorrelation measurements. Standard THz autocorrelation measurements are performed by splitting the THz radiation into two parts and recombining them by using, for example, a Michelson interferometer and measuring the power of the THz radiation. Here, we used a slightly different method (quasi-autocorrelation measurement[16,17]). By using an optical beam splitter, we first split the excitation laser beam into two parts and created double laser pulses. A surface of an InAs wafer was consecutively pumped by the femtosecond laser pulses and the time-correlated THz double pulses were generated. We used a mode-locked Ti:sapphire laser with a central wavelength at 810 nm, pulse duration ~10 fs and repetition frequency of 76 MHz for excitation. The typical output power of the femtosecond laser was 500 mW. By recombining the double THz pulses and measuring the total THz power as a function of the time interval between the two THz pulses, τ, we obtained interferograms of the THz radiation shown in Supplementary Fig. 4.

If the surface of an InAs wafer is consecutively excited with double femotsecond laser pulses exactly at the same position, unwanted artefacts such as interference fringes and bleaching may be induced. To avoid such artefacts, we carefully shifted the positions of the laser excitation in such a way that (1) we do not observe interference fringes in the interferograms, (2) the ratio between the centre peak and the background is as close to 2 as possible, and (3) the obtained interferogram is as symmetric as possible, as shown in Supplementary Fig. 4. By adjusting the optics in such a way, we can generate time-correlated THz double pulses with almost identical waveforms.

Source–drain electrodes with a bowtie antenna geometry. We fabricated the source and drain electrodes of the SMTs in the shape of a bowtie antenna to enhance the coupling efficiency between the THz radiation and the single molecules. The total antenna length was 33 μm and the angle of the bowtie was set to be 57°. Supplementary Figure 5a shows the antenna design pattern and a colour-coded THz field strength calculated at 1.6 THz. As seen in the figure, the radiation at 1.6 THz is enhanced in the nanogap region. Supplementary Figure 5b shows the resonance spectrum of the antenna calculated by using the finite-element method. The antenna has a broad resonance feature around 2 THz and covers a frequency range from 100 GHz up to 4 THz.

Data availability. The data that support the plots within this paper and other findings of this study are available from the corresponding authors upon reasonable request.